Complete microscale profiling of tumor microangiogenesis
A microradiological methodology reveals fundamental aspects of tumor angiogenesis and yields an array of quantitative parameters for its characterization

Chia-Chi Chien [a,b], Ivan M. Kempson [a], Cheng Liang Wang [a], H.H. Chen [a], Yeukuang Hwu [a,b,c],
N.Y. Chen [d], T.K. Lee [a], Cyril Petibois [e], Kelvin K.-C. Tsai [f,*], Ming-Sheng Liu [f], Kwang-Yu Chang [f],
C.S. Yang [g], G. Margaritondo [h,**]

[a] Institute of Physics, Academia Sinica, Nankang, Taipei 115, Taiwan
[b] Department of Engineering and System Science, National Tsing Hua University, Hsinchu 300, Taiwan
[c] Institute of Optoelectronics Sciences, National Taiwan Ocean University, Keelung 202, Taiwan
[d] National Center for High-performance Computing, Hsinchu 300, Taiwan
[e] Université de Bordeaux, CNRS UMR 5248-CBMN, F33405 Talence-Cedex, France
[f] National Institute of Cancer Research and Translational Center for Glandular Malignancies, National Health Research Institutes, Tainan 704, Taiwan
[g] Center for Nanomedicine, National Health Research Institutes, Miaoli 350, Taiwan
[h] Ecole Polytechnique Fédérale de Lausanne (EPFL), CH-1015 Lausanne, Switzerland

ARTICLE INFO

ABSTRACT

Complete profiling would substantially facilitate the fundamental understanding of tumor angiogenesis and of possible anti-angiogenesis cancer treatments. We developed an integrated synchrotron-based methodology with excellent performances: detection of very small vessels by high spatial resolution (~1 μm) and nanoparticle contrast enhancement, *in vivo* dynamics investigations with high temporal resolution (~1 ms), and three-dimensional quantitative morphology parametrization by computer tracing. The smallest (3–10 μm) microvessels were found to constitute >80% of the tumor vasculature and exhibit many structural anomalies. Practical applications are presented, including vessel microanalysis in xenografted tumors, monitoring the effects of anti-angiogenetic agents and *in vivo* detection of tumor vascular rheological properties.

© 2011 Elsevier Inc. All rights reserved.

1. Introduction

Early research on tumor angiogenesis dates back to the 1940s (Kerbel, 2000) and the proposal of therapeutic anti-angiogenesis to the early 1970s (Folkman, 1971). The importance of angiogenesis is widely recognized (Hanahan and Folkman, 1996; Hanahan and Weinberg, 2000), but fundamental aspects are still unclear and the issues about therapy are not solved. Methodology is a relevant hindrance: the ideal objective of a complete three-dimensional (3D) picture of microangiogenesis *in vivo* remained so far elusive. We present here a solution: an integrated approach based on synchrotron microradiology for submicron, real-time analysis and parameterization of tumor microvasculature.

This methodology provides excellent performances compared to current techniques, in terms of spatial resolution (MRI, PET and CT) or sensitivity (MRI) (McDonald and Choyke, 2003; Weissleder, 2002). Its resolution is much better than conventional radiology. Fast imaging (~1 ms per frame) avoids image blurring by live specimen movements. The analysis can be applied to large volumes (several cm^3), i.e., entire tumors and organs.

The methodology also includes tomographic reconstruction—starting from many projection images—that allows 3D profiling (Less et al., 1991) of the microvascular network, down to the smallest vessels (<3 μm) (Hwu et al., 1999). Computer tracing extracts microvasculature characteristics—length, diameter, branching number, angulation and morphological heterogeneities—fundamental in the tumor physiology and development (Palmowski et al., 2008). This 3D examination is a substantial advantage over two-dimensional (2D) shallow (Winkler et al., 2009) analysis by immunohistochemistry.

The methodology requires effective contrast agents. Hydrophobic, hydrophilic, micro-emulsified agents based on high-Z materials and nanoparticles were tested (Chien et al., 2010). Sub-μm BaSO$_4$ particle solutions produced the best contrast without extravascular particle diffusion.

2. Materials and methods

2.1. Reagents and cell culture

The used reagents include Matrigel (BD Biosciences), bevacizumab (Roche). PANC1, A549 cells and WI38 fibroblasts (ATCC) and the immortalized pancreatic stellate cell line, RLT-PSC (a gift from R. Jesnowski) (Jesnowski et al., 2005), were cultured in DMEM (Invitrogen) supplemented with 10% fetal bovine serum and antibiotics. EMT-6 cells and CT-26 cells were separately cultured in Dulbecco modified Eagle medium, (DMEM)-F-12 medium and RPMI-1640 medium (GIBCO, Invitrogen, CA) supplemented with 1% penicillin–streptomycin and 10% heat-inactivated fetal bovine serum (FBS, GIBCO, Invitrogen, CA). The cells were maintained in a humidified incubator with 5% CO_2 at 37 °C.

2.2. Microangiography contrast agents

Several different contrast agents were tested for optimal imaging quality: aqueous solution containing $BaSO_4$ microparticles, PEG-Au nanosol, bare-Au nanosol and emulsified Lipiodol (Chien et al., 2010). The data shown in the article were taken with $BaSO_4$ that provided the best contrast to image the vascular structure without the negative side effects of nanoparticle diffusion.

$BaSO_4$ microparticles were filtered by 5 μm filter (pore size 5 μm; Millex-SV, Millipore, Bedford, Mass). They were then washed with distilled water and centrifuged (3000 g, 60 min). These steps were repeated 3 times. After washing, phosphate buffer saline (PBS) was added. The final concentration of the contrast agent was 30 wt.%.

2.3. Tumorigenesis models

For subcutaneous cancer, 4–5 weeks old mice (BALB/c) provided by the NLAC (National Laboratory Animal Center, Taiwan) were subcutaneously injected in the right leg region with highly metastatic cancer cell strain. The injected 0.1 ml phosphate buffer solution contained $5 \times 10^6 \, ml^{-1}$ of EMT-6 cells.

For metastatic lung cancer, 4–5 weeks old mice (BALB/c) provided by the NLAC were inoculated by tail vein injection with a 0.1 ml volume containing $1 \times 10^7 \, ml^{-1}$ CT-26 cells. The microradiology analysis was performed 14 days after inoculation.

For liver cancer, 4–5 weeks old mice (BALB/c) were provided by the NLAC and inoculated by spleen injection with a 50 μl volume phosphate buffer solution containing $1 \times 10^7 \, ml^{-1}$ CT-26 cells. The microradiology analysis was performed 17 days after inoculation.

For real-time subcutaneous tumor imaging, a PE-05 catheter (BB31695/05, Scientific commodities, Inc., I.D.: 0.2 mm, O.D.: 0.35 mm) was used to inject the contrast agent. The catheter was placed under anesthesia induced by intramuscular injection of 10 μl of Zoletil 50 (50 mg/kg; Virbac Laboratories, Carros, France) per mouse (weight ~20–25 g). The anterior tight skin was incised along a 1 cm^2 circle and the catheter was inserted into the femoral artery and secured by a 6-0 nylon ligature. With the mouse in the X-ray imaging position, one of the aforementioned contrast agents was injected at a 1 μl/s rate. To image the complete tumor region, a number of individual images were patched together; the average time between frames was 50 s.

During imaging, the mice were kept under anesthesia using 1% isoflurane in oxygen. After imaging, the cancerous tissues were removed and embedded in resin for 3D tomography imaging.

For lung cancer and liver cancer imaging, the inferior vena cava was cut and the blood vessel system was flushed with 0.9% normal saline containing heparin (100 units) via a 23G needle inserted into the left ventricle to inject the contrast agent. The injection took 15 min and the flow rate was 1.5 ml/min. Afterwards, 3.7% paraformaldehyde was infused over 25 min with the same flow rate and 30 wt.% $BaSO_4$ was then infused for 1.5 min, again with the same rate.

The orthotopic pancreatic tumorigenesis model (Fig. 2a–c) studies were performed by inoculating pancreatic carcinoma PANC1 cells with or without an identical number of RLT-PSCs (2×10^6 total cells in 100 μl 1:1 mixture of Matrigel and HBSS) into the parenchyma of the pancreatic body of immunodeficient NOD/SCID mice (NLAC). Three days prior to cell implantation, RLT-PSCs were irradiated with 8 Gy of radiation to functionally activate their matrix remodelling and tumor-promoting phenotypes (Jesnowski et al., 2005; Orimo et al., 2005). The mice were sacrificed at 3 days after cell implantation with surgical procedures similar to those for lung and liver cancer. For contrast agent infusion, the PE-10 catheter (BB31695/1, Scientific commodities, Inc., I.D.: 0.28 mm, O.D.: 0.64 mm) was inserted into the thoracic artery and secured by a 6-0 nylon ligature. $BaSO_4$ was then infused for 20 min with a flow rate of 10 μl/s. After perfusing the contrast agent, the cancerous tissues were removed and embedded in resin.

For the xenografted lung tumorigenesis model shown in Fig. 2d–f, A549 cells along with WI-38 pulmonary fibroblasts (1×10^6 cells in 100 μl 1:1 mixture of Matrigel and HBSS) were inoculated subcutaneously into the anterior thighs of NOD-SCID mice. The mice were given intraperitoneal injections of bevacizumab (10 mg/kg) or vehicle at the time of cell implantation and daily thereafter until sacrifice at day 3. The infusion of contrast agent followed the aforementioned procedures.

All the protocols for animal care and experiments related to this article were approved by the Institutional Animal Care and Use Committee (IACUC) of Academia Sinica and National Health Research Institutes, Taiwan.

2.4. Microradiology

The cancerous organs were removed and immersed in 0.9% normal saline solution for 8 h and dehydrated with a series of ethanol solutions (30, 50, 70, 90 and 100%); the immersion and dehydration procedures were repeated three times. Then, the specimen was exposed to a series of resin solutions mixed with ethanol (again 30, 50, 70, 90 and 100%) to replace ethanol with resin. The tissues were then kept in an oven at 70 °C for 8 h for EMbed 812 Resin polymerization.

Synchrotron microradiology (Hwu et al., 1999, 2004a, 2004b; Meuli et al., 2004) was implemented with unmonochromatized (i.e., without filtering to select a narrow band of wavelengths) X-rays emitted by the 01-A beamline wavelength shifter of the National Synchrotron Radiation Research Center (Taiwan). The photon energy ranged from 4 keV to 30 keV and the average beam current in the synchrotron source accelerator was kept constant at 300 mA with the top-up operation mode. To obtain 4.59×3.43 mm images, the X-rays were first converted to visible light by a $CdWO_4$ single crystal scintillator and then captured by an optical microscope with a CCD camera (model 211, Diagnostic instruments, 1600×1200 pixel). The radiation dose was reduced by attenuating the emitted X-ray beam with two pieces of 550 μm single crystalline silicon wafers placed before the animal.

The exposure time was ~100 ms and the distance between the sample and the scintillator was ~5 cm; a 2×, 5× or 10× lens in the optical microscope was used to obtain the desired field of view. The size of each pixel in the final image taken with the 2× lens was ~$2.87 \times 2.86 \, \mu m^2$. For microtomography reconstruction, specimens were fixed by paraformaldehyde and then embedded in resin as described above.

The conceptual details of synchrotron-based microradiology, including absorption and phase contrast, are discussed in Hwu et al. (1999, 2004a, 2004b; Meuli et al., 2004) and in the references therein.

2.5. 3D vessel tracing algorithm

The tracing algorithm was based on the following procedure: first, the image voxels were segmented into several connected clusters. A

cluster is defined as "connected" if every voxel in this cluster is connected through at least one path of connections (two voxels are connected when they are in the 6 nearest neighbouring site, i.e. $x \pm 1$, $y \pm 1$, or $z \pm 1$). Second, image voxels in a connected cluster were encoded based on the idea of region-growth method. Every voxels in this connected cluster was encoded by a number representing the sequential distance of the shortest path from the origin. A codelet i was defined by voxels with coding number $i - 1$, i, $i + 1$ and its center of mass (CM) was calculated based on all these voxels. The tracing for one connected cluster was performed by simply following the codelets sequentially with increasing indices through all the encoded voxels. The skeleton of the image was obtained by connecting all the CMs of each codelet for a segment or branch. When a codelet had disconnected voxels, then it met the branches, i.e. there was a branch point (BP) there. When no further voxels could be traced, then the codelet met the end point (EP). When the codelet reached voxels that had been traced before, then it met a loop, i.e. there was a loop point (LP) there. Finally, after all voxels were traced, the skeleton, BPs, EPs, LPs, cross section area, branch angles and other relevant quantitative parameters for the image could be calculated.

2.6. SOM text

The SOM presents additional images and movies illustrating details of the results of the methodology, essential to appreciate its effectiveness for the different tasks of complete profiling of tumor angiogenesis. The use of video files is particularly important due to the nature of the approach.

3. Results and discussion

We applied the methodology to four types of tumors: subcutaneous, lung, pancreas, and liver. Fig. 1(a–c) shows representative images of subcutaneous cancer taken at different times after injecting the $BaSO_4$ particle solution (Supporting Material S1). Note the fine details of the microvasculature network at an early tumor development stage. The contrast agent amount within the squares is ~86.3 μg for Fig. 1a and 182.3 and 13,498 μg for Fig. 1b and c (all three specimens contained the same total amount).

Fig. 1(d–f) are examples of 3D tomographic imaging: side views of a liver tumor with microangiogenesis confined to its volume (Supporting Material S2). One clearly sees the differences between the cancer microvasculature and the healthy tissue, in particular the microvessel size and density (Supporting Material S3) and the vasculature structure.

Fig. 1g illustrates the extraction of essential 3D microvasculature parameters by *ad hoc* software. The result here is the vessel diameter distribution for the projection image of Fig. 1c.

Fig. 1h is a tomographic cross sectional view of pancreas cancer, with bright spots corresponding to strong contrast agent absorption. After zooming (right), vessels with ~3 μm diameter are clearly detected (these are not artifacts since they are tubular and connected to larger vessels). Thus, our resolution, ~1 μm and 3D analysis can reveal the smallest tumor vessels and measure their geometry for a complete profiling.

The quantitative analysis in 3D was performed with a computer algorithm using the complete data matrix to trace trees or dendritic structures based on the region-growth encoding and codelet with triple codes (Dellian et al., 1996). After tracing the vascular structure, this software automatically yields parameters such as the distributions of vessel sizes, vessel density and branching points (Fig. 1g and Supporting Material S4).

The methodology can detect tiny differences between very similar xenografted tumors, as shown by the analysis of stroma-mediated tumors (Kuperwasser et al., 2004; Orimo et al., 2005) in Fig. 2 (and Supporting Material S5). Pancreatic carcinoma PANC1 cells and pancreatic
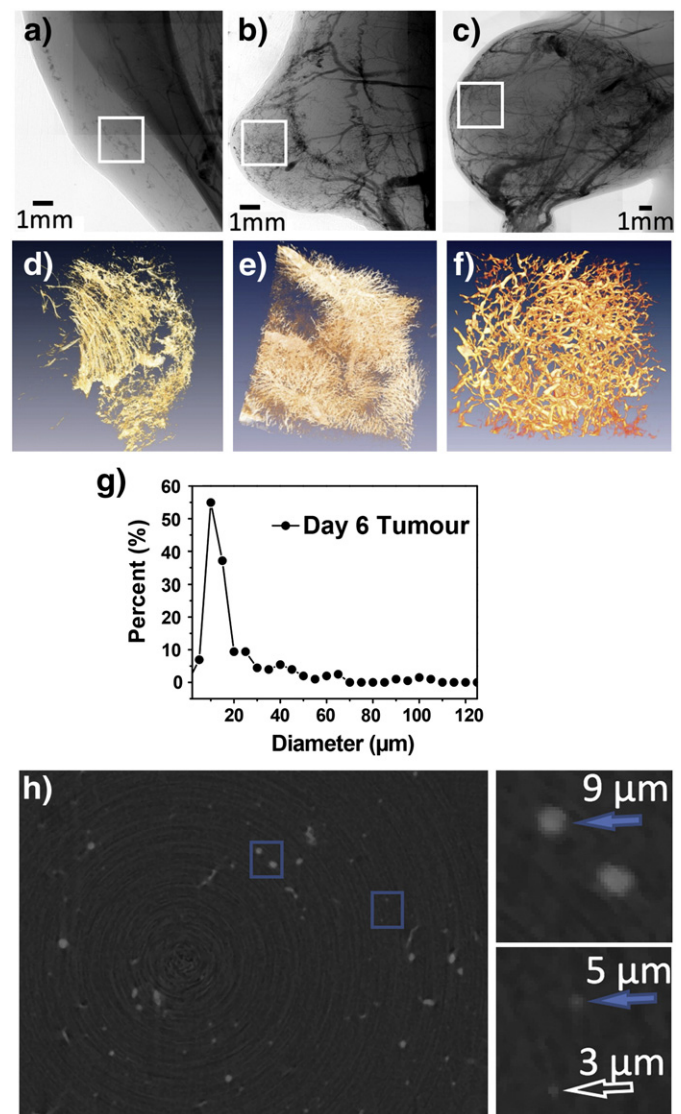

Fig. 1. (a)–(c): X-ray microimages of subcutaneously implanted cancer tumors in the thighs of three different mice, 3, 6 and 15 days after injection; anomalous microvasculature details become clear after 6 days. (d) Tomographically reconstructed side-view (4.59 mm × 3.43 mm, 15 days after injection) showing differences between the tumor vessels and the underlying normal tissue. (e), (f): magnified (924 μm × 684 μm) pictures of healthy liver tissue (e) and anomalous angiogenesis in a cancer region (f). (g) Microvessels size distribution in the square of (c) with a high percentage of diameters ≤10 μm in. (h) 702 μm × 507 μm (left) and 50 μm × 50 μm (right) tomographically reconstructed slices showing vessels in pancreas cancer. The magnified images reveal very small vessels (9, 5 and 3 μm).

stromal stellate cells (RLT-PSCs)—activated by ionizing radiation (Jesnowski et al., 2005) (RAS specimen) or not irradiated (control (Ctrl) specimen)—were orthotopically co-implanted into the pancreatic parenchyma. Compared to the normal tissue of Fig. 2a, images taken 3 days after implantation, Fig. 2b and c, show the exuberant microvascular network surrounding the inoculation site.

Computer analysis (Supporting Material S6) unveils very small differences between the RAS and Ctrl specimens. Fig. 2d shows that ~61% and ~38% of the vessel segments (between branch points) for the Ctrl specimen have diameters <10 μm and <5 μm; the RAS specimen values are ~71% and ~46%. Fig. 2e shows that 72% (Ctrl) and 67% (RAS) of the vessels are shorter than 75 μm. Thus, the RAS specimen has shorter and narrower branches.

The vessel "tortuosity" is quantitatively described by the ratio of the vessel length between branch points to their distance. Fig. 2f shows that for the Ctrl and RAS specimens 25% and 23% of the
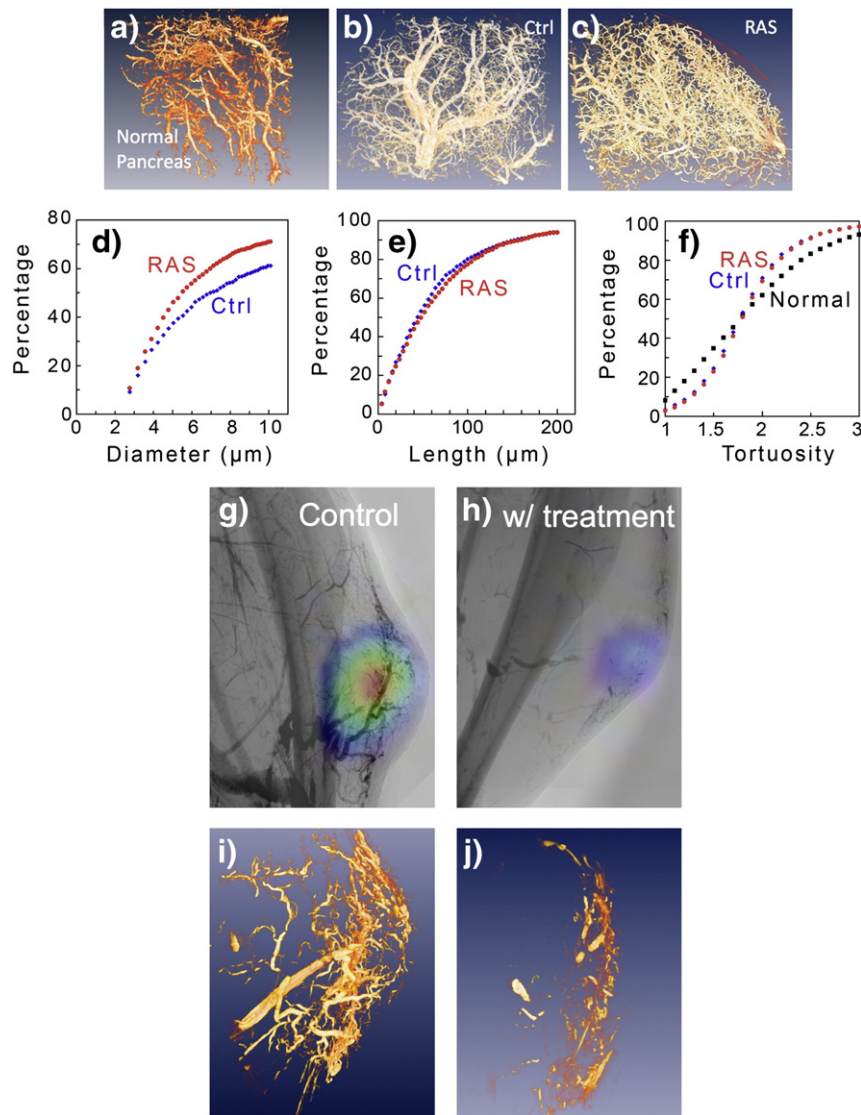
Fig. 2. Stroma-mediated tumor microangiogenesis and its changes by bevacizumab. (a)–(c): Tomographically reconstructed microvasculature images for orthotopic pancreatic cancer: (a) normal pancreas; (b) and (c): 3 days after implanting PANC1 cells into the pancreatic parenchyma of NOD-SCID mice without (Ctrl) or with (RAS) radiation activation. Field of view (reconstructed box): 924 μm × 684 μm. (d) Percentage of vessels in (b) and (c) with diameter smaller than the horizontal scale value. (e) Percentage of vessels with length between adjacent branches smaller than the horizontal scale value. (f) "Tortuosity", measured as the ratio of the vessel length to the distance between branch points; the plot shows the percentage of cases in which the ratio is smaller than the horizontal scale value. (g), (h): 6 mm × 8.8 mm images of xenografted NSCLC tumor treated with bevacizumab (10 mg/kg per day for 3 days) (h) or vehicle (g). Bioluminescence maps showing the tumor location are superimposed. (i), (j): Tomographically reconstructed 0.75 mm × 1 mm images corresponding to (g) and (h).

vessels has a ratio <1.5. The portion is 35% for normal tissue, thus the cancer microvasculature is substantially more tortuous than normal pancreas. Other extracted parameters are the total number of branch points, starting points, end points and loop points. The corresponding results are larger for RAS than for Ctrl by ~9.6%, ~17.8%, ~30.1% and ~9.9%.

The quantitative 3D analysis, like the imaging and the tomographic reconstruction, can be extended to whole tumors and entire organs. We find that the anomalous vasculature typically occupies ~3–4% of total tissue volume (Supporting Material S7).

The methodology is suitable to detect the impact of anti-angiogenesis agents like the (VEGF)-blocking agent bevacizumab (Zerbini et al., 2008). On a nude mice model, subcutaneous tumors induced by A549 lung cancer cells were analyzed with or without intraperitoneal administrations of bevacizumab. Retroviral labelling of the A549 cells with firefly luciferase visualized the tumor by bioluminescence imaging (BLI). Fig. 2f shows large angiogenic tumors near and within the BLI signal 3 days after cell inoculation.

Bevacizumab does significantly affect the observed angiogenesis (Fig. 2g) (Helmlinger et al., 1997; Jain, 1999). A computer analysis of tomography images, Fig. 2h and i, reveals indeed differences in the vasculature morphology (Supporting Material S8): the vessels are larger, longer and less tortuous after bevacizumab treatment.

The methodology can image *in vivo* the microvasculature flow dynamics in growing tumors (Elleaume et al., 2000; Hwu et al., 2004b; Kim et al., 2007; Myojin et al., 2007). Fig. 3 is a sequence revealing the contrast agent flow adjacent to a subcutaneously implanted tumor (the same as in Fig. 1c). We monitored the contrast agent accumulation with time in different tumor regions and the surrounding stroma through the pixel intensity of the tomographic images, corresponding to the X-ray absorption and proportional to the contrast agent amount. After injecting the agent, this intensity first increases (Fig. 3b and e and Supporting Material S9) and then saturates (Fig. 3f and g).

The contrast agent initially accumulates in a small stroma region (Fig. 3d, arrow). Note that some microvasculature areas are more
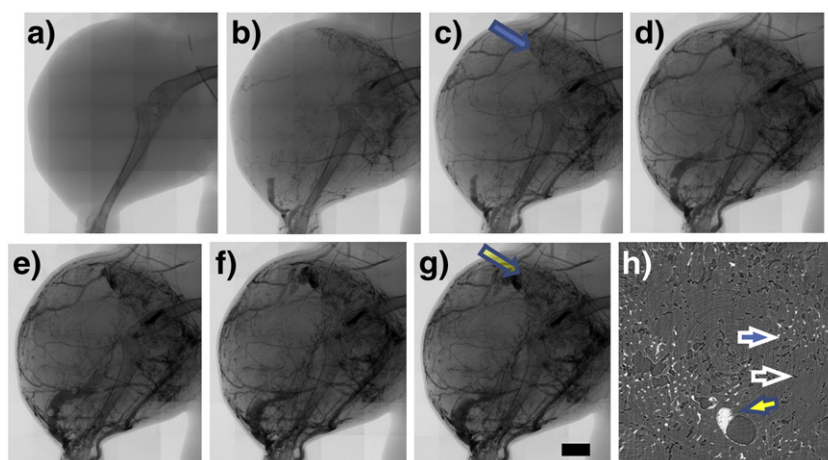
Fig. 3. Micrographs from an image sequence (50 s intervals) reveal the contrast agent flow in the microvasculature of a subcutaneously implanted tumor. The arrow in (c) marks a vessel filled with contrast agent later than the others, already visible in (b). The arrow in (g) marks a blood-pool-like area with high contrast agent accumulation (scale bar: 1 mm). (h) Reconstructed slice (0.924 mm × 0.924 mm) of healthy mouse liver showing vessels with the incomplete contrast agents filling.

easily perfused by the blood stream than others—a valuable information for understanding the tumor mass viability (Sahai, 2005). One sees cell invasivity where vasculature is dense and functional and hypoxic areas where it is underdeveloped and/or less functional.

High magnification shows that the local contrast agent accumulation is not due to clustered vessels but to extravasation (Roberts and Palade, 1997), likely related to the altered permeability of tumor microvessels—and to the well known capillary fenestration after strong angiogenic stress in tumor areas (Hobbs et al., 1998). We do not observe accumulation in normal tissues. The methodology thus identifies tumor areas where fenestration occurs, which is considered a major facilitator of tumor development (Roberts and Palade, 1997) and potentially of targeted drug delivery (Deeken and Loscher, 2007).

Finally, the methodology can also detect unfilled microvessels. In this case (Fig. 3h), phase contrast (Hwu et al., 2004a, 2004b; Meuli et al., 2004) modulates the intensity at the vessel boundary delineating the walls—prevailing over absorption contrast. This facilitates, for example, the detection of circulation dynamics inhomogeneities.

In essence, complete profiling of tumor microangiogenesis requires 2D and 3D imaging down to micron-size vessels and over entire tumors, evaluation of quantitative parameters characterizing the microvessel network and time-resolved analysis of the anomalous blood dynamics. The methodology here described fully meets all of these requirements. It can thus be used to clarify the microvascular aspects of tumor growth at early and advanced stages, and its possible exploitation for therapy.

Acknowledgments

Appendix A. Supplementary data

Supplementary data to this article can be found online at doi:10.1016/j.biotechadv.2011.12.001.

References

Chien CC, Wang CH, Wang CL, Li ER, Lee KH, Hwu Y, et al. Synchrotron microangiography studies of angiogenesis in mice with microemulsions and gold nanoparticles. Anal Bioanal Chem 2010;397:2109–16.

Deeken JF, Loscher W. The blood–brain barrier and cancer: transporters, treatment, and Trojan horses. Clin Cancer Res 2007;13:1663–74.

Dellian M, Witwer BP, Salehi HA, Yuan F, Jain RK. Quantitation and physiological characterization of angiogenic vessels in mice: effect of basic fibroblast growth factor, vascular endothelial growth factor/vascular permeability factor, and host microenvironment. Am J Pathol 1996;149:59–71.

Elleaume H, Fiedler S, Esteve F, Bertrand B, Charvet AM, Berkvens P, et al. First human transvenous coronary angiography at the European Synchrotron Radiation Facility. Phys Med Biol 2000;45:L39–43.

Folkman J. Tumor angiogenesis: therapeutic implications. N Engl J Med 1971;285: 1182–6.

Hanahan D, Folkman J. Patterns and emerging mechanisms of the angiogenic switch during tumorigenesis. Cell 1996;86:353–64.

Hanahan D, Weinberg RA. The hallmarks of cancer. Cell 2000;100:57–70.

Helmlinger G, Yuan F, Dellian M, Jain RK. Interstitial pH and pO2 gradients in solid tumors in vivo: high-resolution measurements reveal a lack of correlation. Nat Med 1997;3:177–82.

Hobbs SK, Monsky WL, Yuan F, Roberts WG, Griffith L, Torchilin VP, et al. Regulation of transport pathways in tumor vessels: role of tumor type and microenvironment. Proc Natl Acad Sci U S A 1998;95:4607–12.

Hwu Y, Hsieh HH, Lu MJ, Tsai WL, Lin HM, Goh WC, et al. Coherence-enhanced synchrotron radiology: refraction versus diffraction mechanisms. J Appl Phys 1999;86: 4613–8.

Hwu Y, Tsai WL, Chang HM, Yeh HI, Hsu PC, Yang YC, et al. Imaging cells and tissues with refractive index radiology. Biophys J 2004a;87:4180–7.

Hwu Y, Tsai WL, Je JH, Seol SK, Kim B, Groso A, et al. Synchrotron microangiography with no contrast agent. Phys Med Biol 2004b;49:501–8.

Jain RK. Understanding barriers to drug delivery: high resolution in vivo imaging is key. Clin Cancer Res 1999;5:1605–6.

Jesnowski R, Furst D, Ringel J, Chen Y, Schrodel A, Kleeff J, et al. Immortalization of pancreatic stellate cells as an in vitro model of pancreatic fibrosis: deactivation is induced by matrigel and N-acetylcysteine. Lab Invest 2005;85:1276–91.

Kerbel RS. Tumor angiogenesis: past, present and the near future. Carcinogenesis 2000;21:505–15.

Kim JW, Seo HS, Hwu Y, Je JH, Kim A, Oh CW, et al. In vivo real-time vessel imaging and ex vivo 3D reconstruction of atherosclerotic plaque in apolipoprotein E-knockout mice using synchrotron radiation microscopy. Int J Cardiol 2007;114:166–71.

Kuperwasser C, Chavarria T, Wu M, Magrane G, Gray JW, Carey L, et al. Reconstruction of functionally normal and malignant human breast tissues in mice. Proc Natl Acad Sci U S A 2004;101:4966–71.

Less JR, Skalak TC, Sevick EM, Jain RK. Microvascular architecture in a mammary carcinoma: branching patterns and vessel dimensions. Cancer Res 1991;51:265–73.

McDonald DM, Choyke PL. Imaging of angiogenesis: from microscope to clinic. Nat Med 2003;9:713–25.

Meuli R, Hwu Y, Je JH, Margaritondo G. Synchrotron radiation in radiology: radiology techniques based on synchrotron sources. Eur Radiol 2004;14:1550–60.

Myojin K, Taguchi A, Umetani K, Fukushima K, Nishiura N, Matsuyama T, et al. Visualization of intracerebral arteries by synchrotron radiation microangiography. AJNR Am J Neuroradiol 2007;28:953–7.

Orimo A, Gupta PB, Sgroi DC, Arenzana-Seisdedos F, Delaunay T, Naeem R, et al. Stromal fibroblasts present in invasive human breast carcinomas promote tumor growth and angiogenesis through elevated SDF-1/CXCL12 secretion. Cell 2005;121:335–48.

Palmowski M, Huppert J, Hauff P, Reinhardt M, Schreiner K, Socher MA, et al. Vessel fractions in tumor xenografts depicted by flow- or contrast-sensitive three-dimensional high-frequency Doppler ultrasound respond differently to antiangiogenic treatment. Cancer Res 2008;68:7042–9.

Roberts WG, Palade GE. Neovasculature induced by vascular endothelial growth factor is fenestrated. Cancer Res 1997;57:765–72.

Sahai E. Mechanisms of cancer cell invasion. Curr Opin Genet Dev 2005;15:87–96.

Weissleder R. Scaling down imaging: molecular mapping of cancer in mice. Nat Rev Cancer 2002;2:11–8.

Winkler F, Kienast Y, Fuhrmann M, Von Baumgarten L, Burgold S, Mitteregger G, et al. Imaging glioma cell invasion in vivo reveals mechanisms of dissemination and peritumoral angiogenesis. Glia 2009;57:1306–15.

Zerbini G, Lorenzi M, Palini A. Tumor angiogenesis. N Engl J Med 2008;359:763. author reply 764.